SCHOOL OF PHYSICS AND ASTRONOMY

YEAR 4 PROJECT DISSERTATION

SESSION 2020-2021

Name:	**Ryan Alexander**
Student Number:	**1769257**
Degree Programme:	**MPhys Physics**
Project Title:	**Exploring Models for Time-Dependent Refractive Index Materials and Confirming the Temporal Snell's Law of Time-Refraction with Finite-Difference Time-Domain Simulations**
Supervisor:	**Dr DM Beggs**
Primary Assessor:	**Dr H Deng**
Second Assessor:	**Dr SS Oh**

Declaration:

I have read and understand Appendix 2 in the Student Handbook: "Some advice on the avoidance of plagiarism".

I hereby declare that the attached report is exclusively my own work, that no part of the work has previously been submitted for assessment (although it may re-use material from the "Summary Report" for **this project** as it is considered part of the same assessment), and that I have not knowingly allowed it to be copied by another person.

Exploring Models for Time-Dependent Refractive Index Materials and Confirming the Temporal Snell's Law of Time Refraction with Finite-Difference Time-Domain Simulations

Ryan Alexander - C1769257

Submitted May 2021

Abstract

The ultrafast time refraction of light was explored by simulating pulses in materials with a temporally changing refractive index. Two models were used for the time-dependence of the refractive index, each modelling a realistic mechanism for the refractive index change. Both red-shifts and blue-shifts due to time refraction were demonstrated with frequency shifts of +100% to -50% of input frequency. These shifts were not adiabatic but can be generalised to adiabatic frequency conversion. Both models demonstrated frequency shifts that were found to agree to better than 96% (and up to 99.8%) with analytical predictions provided by a temporal equivalent of Snell's law.

Contents

Acknowledgements

I would like to thank my supervisor, Dr. Daryl Beggs for helping me to develop my scientific project performing skills for two years in a row and for providing technical guidance on this project.
I would also like to thank my parents for their continuous support throughout my degree which has culminated in this project.

1 Aims

This project aimed to demonstrate the frequency shifts of "probe" light pulses subject to temporal changes in a material's refractive index using finite-difference time-domain simulations of pump-probe experiments. For two realistic models of time-dependent refractive index changes, the project aimed to demonstrate a frequency shift due to time refraction and explore how factors such as medium length and pump-probe delay affected this shift. Finally, the project aimed to confirm that a temporal equivalent of Snell's law predicts the frequency shifts observed to high accuracy for both models.

2 Theory and Literature Review

2.1 The Concept of Time Refraction

Physicists are familiar with Snell's law of refraction which governs the change in the propagation direction of light at a spatial boundary between two refractive indices. Theoretically, however, a spatially homogeneous material with a time-dependent refractive index can be imagined. If light was passed through this material while its refractive index was changing, the light would be passing through a temporal refractive index boundary.

Physicists have discovered a multitude of ways to derive the original Snell's law governing spatial boundaries. In 2001 however, a paper developed a temporal analogue for Snell's law which is expected to govern light passing through a temporal refractive index boundary [1]. This derivation is worked through in section 2.2.

2.2 Temporal Snell's Law Derivation

2.2.1 The Electromagnetic Wave Equation

First, the electromagnetic wave equation is derived. Maxwell's equations for a region of space, free of charges and currents, are considered in the form shown in equations 1, 2 and 3. $\mathbf{E}$ and $\mathbf{B}$ are the electric and magnetic fields respectively, ε_0 and μ_0 are the permittivity and permeability of free space respectively and t is time:

$$\nabla \times \mathbf{E} + \frac{\partial \mathbf{B}}{\partial t} = 0 \tag{1}$$

$$\nabla \times \mathbf{B} - \mu_0 \varepsilon_0 \frac{\partial \mathbf{E}}{\partial t} = 0 \tag{2}$$

$$\nabla \cdot \mathbf{E} = 0 \tag{3}$$

Taking the curl of equation 1, using the vector calculus identity $\nabla \times (\nabla \times \mathbf{V}) = \nabla (\nabla \cdot \mathbf{V}) - \nabla^2 \mathbf{V}$ and substituting in equations 2 and 3, gives the electromagnetic wave equation derived in

equation 4:

$$\nabla \times (\nabla \times \mathbf{E}) + \frac{\partial}{\partial t} (\nabla \times \mathbf{B}) = 0$$

$$\nabla (\nabla \cdot \mathbf{E}) - \nabla^2 \mathbf{E} + \frac{\partial}{\partial t} (\nabla \times \mathbf{B}) = 0$$

$$\nabla \cdot \mathbf{E} = 0 \implies \nabla^2 \mathbf{E} + \frac{\partial}{\partial t} (\nabla \times \mathbf{B}) = 0 \tag{4}$$

$$\nabla \times \mathbf{B} = \mu_0 \varepsilon_0 \frac{\partial \mathbf{E}}{\partial t} \implies \nabla^2 \mathbf{E} + \mu_0 \varepsilon_0 \frac{\partial^2 \mathbf{E}}{\partial t^2} = 0$$

2.2.2 Plane Wave Solutions

Equation 4, the general wave equation, is satisfied by sinusoidal plane waves of the form shown in equation 5. Where $\mathbf{r}$ is a spatial vector from the origin, t is time, $\mathbf{k}$ is the wave-vector defining the planar wavefronts and ω is the angular frequency:

$$\mathbf{E}(\mathbf{r}, t) = \exp\left[i\left(\mathbf{k} \cdot \mathbf{r} - \omega t\right)\right], \qquad k = \frac{\omega}{c} n \tag{5}$$

$\mathbf{k}$ and ω are governed by the dispersion relation: $|\mathbf{k}| = k = \frac{\omega}{c} n$, where k is the wavenumber, c is the speed of light and n is the refractive index of the medium.

2.2.3 Refractive Index Boundaries

Considering an electromagnetic plane wave (equation 5) travelling through a material with a refractive index of n_1 at times $t < 0$ and n_2 at times $t > 0$, the wave can be split into three separate plane waves, equations 6, 7 and 8.
The incident plane wave, for $t < 0$:

$$\mathbf{E}_i(\mathbf{r}, t) = \exp\left[i\left(\mathbf{k} \cdot \mathbf{r} - \omega_i t\right)\right], \qquad k = \frac{\omega_i}{c} n_1 \tag{6}$$

The transmitted and a reflected plane wave, for $t > 0$:

$$\mathbf{E}_t(\mathbf{r}, t) = \exp\left[i\left(\mathbf{k} \cdot \mathbf{r} - \omega_t t\right)\right], \qquad k = \frac{\omega_t}{c} n_2 \tag{7}$$

$$\mathbf{E}_r(\mathbf{r}, t) = \exp\left[i\left(\mathbf{k} \cdot \mathbf{r} - \omega_r t\right)\right], \qquad k = \frac{\omega_r}{c} n_2 \tag{8}$$

From the dispersion relations of the incident and transmitted waves (equations 6 and 7) and the fact that frequency (f) and angular frequency are directly proportional, a temporal analogue to Snell's law is derived in equation 9:

$$k = \frac{\omega_i}{c} n_1 = \frac{\omega_t}{c} n_2$$

$$\omega_i n_1 = \omega_t n_2 \tag{9}$$

$$\omega = 2\pi f \implies \quad f_i n_1 = f_t n_2$$

This temporal Snell's law (equation 9) implies that instead of transmitted light experiencing a change in propagation direction, as in spatial refraction, the transmitted light experiences a frequency conversion: $f_t = f_i \left(n_1/n_2\right)$. In the case of spatial refractive index boundaries the same derivation is performed except k is varied within the dispersion relations instead of ω ($k_i = \omega/(cn_1), k_t = \omega/(cn_2), k_r = \omega/(cn_1)$).

A more intuitive understanding of the cause of the frequency conversion implied by the temporal Snell's law (equation 9) can be attained by considering the spacetime diagrams of wavefronts (shown as arrows) passing across a boundary between two refractive indices shown in figure 1:
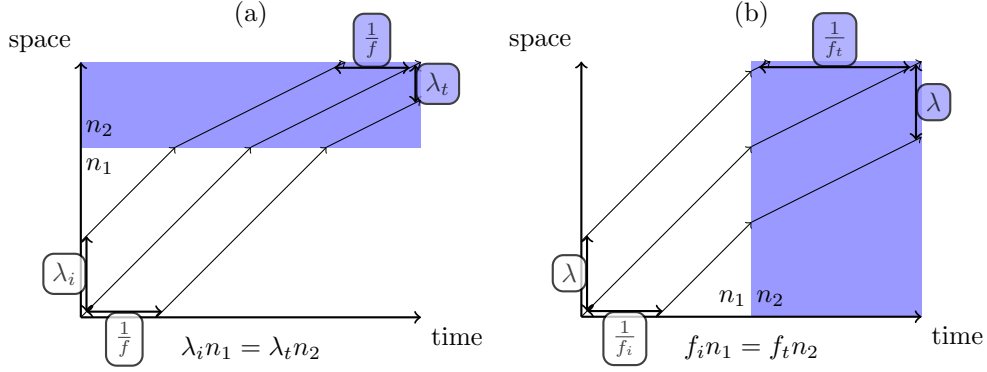
Figure 1: Two spacetime diagrams showing the world-lines of periodic wavefronts (three thin arrows) subject to refractive index boundaries between n_1 and n_2. Diagram "(a)" shows wavelength conversion and frequency conservation for light subject to a spatial refractive index boundary. Diagram "(b)" shows wavelength conservation and frequency conversion for light subject to a temporal refractive index boundary. Recreation from [2].

The temporal Snell's law has been shown for a step function in refractive index but it is assumed to hold for smooth changes in refractive index too. This is the case in spatial refractive index boundaries i.e. Snell's law is the same for a graded-index boundary (a smooth spatial change in index) as it is for a spatial step function in refractive index.

2.3 Mechanisms to Change Refractive Index

The main challenge in demonstrating time refraction is the high speed at which light propagates through a material. Light travels through materials on the order of picoseconds (10^{-12}s) per millimetre of material. Most methods for controlling refractive index can only be implemented homogeneously in small volumes of material. Therefore, to observe time refraction, the refractive index of a material must be varied significantly on the pico or femtosecond order. This area of physics is named "ultrafast optics" owing to the requirement for pico and femtosecond dynamic changes in materials. Multiple methods for achieving this ultrafast variation of the refractive index have been developed.

2.3.1 Plasma

Time-dependent refractive indices were first studied extensively in plasmas, starting in 1996 [3]. Fundamentally, the refractive index of a material is a function of its electric permittivity (ε) and magnetic permeability (μ) [4]:

$$n = \sqrt{\varepsilon \mu} \tag{10}$$

In non-stationary plasmas, electron density can vary on the ultra-fast timescale, resulting in a time-varying electric permittivity and hence a time-varying refractive index [5]. This is analogous to different densities of air having different refractive indices. Frequency shifts of $\Delta f / f \approx 1\%$ have been demonstrated in non-stationary plasmas with transmission efficiencies of up to 60% [6].

2.3.2 Free Carrier Dispersion

Another more widely researched implementation of frequency-conversion using time-dependent refractive indices has been free carrier dispersion. By injecting or exciting free carriers into/in a semiconductor, the carrier density and hence the refractive index of the semiconductor can be controlled according to equation 11 [7]:

$$\Delta n = \frac{-e^2 \lambda^2}{8\pi^2 c^2 \varepsilon_0 n_1} \left(\frac{N_e}{m_{ce}^*} + \frac{N_h}{m_{ch}^*} \right) \tag{11}$$

6

In equation 11, m_{ce}^* and m_{ch}^* are the effective masses of holes and electrons respectively (can be treated as constants) and e is the charge of an electron, ε_0 is the permittivity of free space, n_1 is the refractive index of the unperturbed material, λ is the wavelength of light (in free space) and N_e and N_h are the free carrier concentrations of electrons and holes respectively. The increase in free carriers is most commonly achieved by promoting carriers across the valence-conductance band gap with a sufficiently high frequency light pulse via either single-photon or two-photon absorption. This method is practical in materials, such as silicon, which could be incorporated into integrated photonic circuits [8]. $\Delta f/f \approx 0.1\%$ frequency shifts have been achieved in waveguides with efficiencies of up to 80% by free carrier dispersion [9, 10]. Ultrafast (picosecond) laser "switching pulses" are needed to excite carriers to achieve this dynamic change in refractive index, while the free carriers decay on the nanosecond order [10]. The primary limitation of this method is free carrier absorption of the incident light pulse. Free carriers not only affect the refractive index but also the absorptivity of a material. The absorption (intensity loss in dBcm^{-1}) of a material is given by equation 12 [11]:

$$\Delta\alpha = \frac{-e^3\lambda^2}{4\pi^2 c^3 \varepsilon_0 n_1}\left(\frac{N_e}{\mu_e\left(m_{ce}^*\right)^2} + \frac{N_h}{\mu_h\left(m_{ch}^*\right)^2}\right) \tag{12}$$

μ_e and μ_h are the electron and hole mobilities respectively. Equations 11 and 12 show that while greater frequency shifts could be obtained by increasing the carrier concentration within materials, the efficiency of the frequency shift can quickly drop. Experiments have shown increasing Δn to rapidly reduce efficiency to below 20% [8].

2.3.3   The Optical Kerr Effect

The optical Kerr effect, which does not suffer from increasing loss as Δn is increased, can also be used to rapidly change the refractive index of a material. When a material is subject to intense light its refractive index increases according to equation 13 [12]:

$$\Delta n = \frac{3\chi^{(3)}}{4n_1^2\varepsilon_1 c}I \tag{13}$$

In equation 13, the subscript 1 denotes the properties of the unperturbed material, with no incident light. $\chi^{(3)}$ is a tensor describing the proportionality between an applied electric field and the resultant polarisation of a material named the third order susceptibility [13] (it will be treated as a constant hereafter) and I is the time-averaged intensity of the incident light. Equation 13 implies that Δn is directly proportional to intensity. Implementations of the optical Kerr effect (also referred to as cross-phase modulation (XPM)) have shown frequency shifts of up to $\Delta f/f \approx 1\%$ [14–17].

2.4   Adiabatic Frequency Conversion

2.4.1   True Adiabaticity

The concept of adiabaticity has, relatively recently, been extended to the frequency conversion of light within a system. In this context, adiabaticity is the conversion of one mode to another without the excitation of other modes (e.g. reflections). When the frequency of light in a system is varied slow enough relative to the spacing between wavelengths supported by the system $\left(df/dt \ll 1/f_n - 1/f_{n+1}\right)$, all of the light is frequency converted to the expected frequency [9, 18, 19]. In other words, an instantaneous change (step function) of refractive index will convert the frequency of light non-adiabatically, while a sufficiently gradual and smooth change of refractive index will convert the light adiabatically [2]. This is analogous to how non-reflective coatings provide a system with a more gradual change in refractive index across space to achieve adiabaticity.

In this project, light is simulated travelling through an infinitely large 2D material. This means that the supported frequencies of the system are continuous and no change in index is gradual

enough to achieve adiabatic frequency conversion $\left(df/dt > 0\right)$. Theoretically, a finite resonant structure, supporting discrete modes, could be used to investigate adiabatic frequency conversion. Adiabatic frequency conversion via time-refraction has been achieved using resonant structures, showing frequency conversions of up to $\Delta f/f \approx 0.15\%$ [20]. Achieving adiabatic frequency conversion is outside the scope of this project, however, as the temporal Snell's law holds for adiabatic and non-adiabatic processes, the results presented in this report can be generalised to both adiabatic and non-adiabatic frequency conversion.

2.4.2 Previous Demonstrations

In time-refraction the phrase "adiabatic frequency conversion" is used to describe efficient frequency conversion. Very few papers demonstrating frequency conversion have considered whether the conversion is "truly adiabatic" or not. Frequency shifts due to the time-refraction of light have been demonstrated a multitude of times [8–10, 14–17, 20–22], but with very limited Δf as detailed in sections 2.3.2 and 2.3.3. Many demonstrations of frequency shift via free carrier dispersion and the optical Kerr effect make use of "slow light" (light with very low group velocity) [9, 21] or a resonating cavity which traps light [8, 22] which significantly reduces transmission efficiency [20]. These are required because the dynamic changes in refractive index are not quick enough to impose a significant frequency shift on light moving at "normal" speeds through a practically sized material. Even with these methods frequency shifts have been limited to $\Delta f/f \approx 1\%$.

2.5 Timeliness and Potential

2.5.1 Epsilon-Near-Zero Materials

A 2017 paper [23] introduces the concept of using epsilon-near-zero metamaterials (man-made materials with abnormal properties) to achieve relative refractive index changes of ± 2.5 via the optical Kerr effect where previously no "unity order" refractive index changes were possible. These large refractive index variations are achieved by designing a metamaterial with $\varepsilon \ll 1$, hence $\varepsilon_1^2 \mu_1 = n_1^2 \varepsilon_1 \to 0$ in equation 13 and Δn is amplified. A 2020 paper [2] implements an indium tin oxide (ITO) film which has an electric permittivity of close to 0 at 1200-1300nm wavelengths. The thickness of the ITO film was only 620nm, resulting in the 120fs pulse never residing fully within the film and only being subject to a fraction of Δn. Despite this limitation, frequency shifts of up to $\frac{\Delta f}{f} \approx 6\%$ were achieved. It can be seen from equation 11 that a low ε and a subsequent low n_1 could have a similar amplifying effect on the frequency shift achieved by free carrier dispersion (although a proportional decrease in efficiency would be suffered according to equation 12).

2.5.2 Potential

The recent break-through in using epsilon-near-zero materials has created a possibility for efficient, high Δf frequency conversion via time-refraction. Time-refraction could find application in on-chip photonic circuits, for example multiplexing in optical communications or even optical quantum computing.

3 Methodology

3.1 Pump-Probe Experiments

When studying the ultra-fast optical effects of light pulses on materials a pump-probe experiment is required. The pump refers to the light pulse that induces a change in the material's properties. The probe refers to the light pulse that is passed through the material to determine the material's optical properties. Observations of time-refraction have been achieved almost exclusively through the use of pump-probe experiments [2, 8, 9, 14–17]. In this project materials with time-varying refractive indices are modelled such that they behave as though a pump pulse is incident on

them. Probe pulses are also passed through the material and detected after being subject to the materials' properties. Hereafter the delay between the emission of the probe pulse and the change in the material's properties will be referred to as the "pump-probe delay".

3.2 Finite-Difference Time-Domain Simulations

To simulate the propagation of light accurately a "computer-solvable" method for approximating Maxwell's equations is needed.

3.2.1 Finite-Difference Methods

Finite-difference methods are numerical methods for approximating solutions to differential equations. Consider $f(x)$, an arbitrary smooth function whose derivative is to be approximated. The Taylor series (equation 14) allows for $f(x) = f(x_0 + h)$ (where h is a real, positive number) to be expressed as a function of $f(x_0)$ and its derivatives (where $f^{(n)}$ is the nth derivate of f with respect to x) [24]:

$$f(x_0 + h) = f(x_0) + h\frac{f'(x_0)}{1!} + h^2\frac{f^{(2)}(x_0)}{2!} + \cdots + h^n\frac{f^{(n)}(x_0)}{n!} + \cdots \tag{14}$$

For small h, Equation 14 can be truncated to give equation 15:

$$\begin{aligned} h \to 0 \implies h^2\frac{f^{(2)}(x_0)}{2!} + \cdots + h^n\frac{f^{(n)}(x_0)}{n!} + \cdots \approx 0 \\ \implies f(x_0 + h) \approx f(x_0) + hf'(x_0) \end{aligned} \tag{15}$$

A similar approximation for $f(x_0 - h)$ is also considered in equation 16:

$$\begin{aligned} f(x_0 - h) = f(x_0) - h\frac{f'(x_0)}{1!} - h^2\frac{f^{(2)}(x_0)}{2!} - \cdots - h^n\frac{f^{(n)}(x_0)}{n!} - \cdots \\ h \to 0 \implies f(x_0 - h) \approx f(x_0) - hf'(x_0) \end{aligned} \tag{16}$$

Equations 15 and 16 can be combined to obtain a central difference equation for the first derivative of a function $f(x_0)$ shown in equation 17:

$$f'(x_0) = \lim_{h \to 0} \frac{f(x_0 + h) - f(x_0 - h)}{2h} \tag{17}$$

The fact that equation 17 uses only discrete values of $f(x)$ to find $f'(x_0)$ means that a computer can be used to solve it very quickly.

3.2.2 Finite-Difference Time-Domain for Solving Maxwell's Equations

The central difference equation (equation 17) can be applied to Maxwell's equations [25, 26]. For example, consider an electromagnetic plane wave propagating in the z-direction, with polarisation such that $\mathbf{E} = (E_x(t, z), 0, 0)$ and $\mathbf{B} = (0, B_y(t, z), 0)$. Such a wave would be subject to equation 18:

$$\begin{aligned} \nabla \times \mathbf{E} = -\frac{\partial \mathbf{B}}{\partial t} \\ \frac{\partial E_x}{\partial z} = -\frac{\partial B_y}{\partial t} \end{aligned} \tag{18}$$

The evolution of the magnetic field ($\mathbf{B}$) in equation 18, can be approximated using equation 17, giving equation 19.

$$\frac{\partial B_y(z)}{\partial t} = -\frac{E_x(z + \Delta z) - E_x(z - \Delta z)}{2\Delta z} \tag{19}$$

Next, $\partial E_x/\partial z$ is approximated in a similar manner, using a time step of Δt to approximate $\partial B_y/\partial t$. This alternating method can then be performed for the desired span of z and t values.

3.2.3 Lumerical FDTD

The program Lumerical FDTD allows users to solve Maxwell's equations using the finite-difference time-domain method described in section 3.2.2 across arbitrarily large areas and across arbitrarily large amounts of time. A user specified mesh of Δx, Δy, Δz and Δt are used as the spatial and temporal "steps" (h) in the finite-difference method (equation 17). Users can also add materials with user-defined optical properties (e.g. refractive index) to the simulation region, which modify Maxwell's equations. In this project Lumerical FDTD is used to simulate light propagating through a material with a time-dependent refractive index.

Because the central difference equations converge exactly on Maxwell's equations, without approximations, finite-difference time-domain simulations are considered "numerical experiments" with small errors depending on Δx, Δy, Δz and Δt.

3.3 Simulation Components

To explore time-refraction, simulations comprised of a time-dependent refractive index material, a plane wave source and a detector are used. Plane waves serve as the simplest form of light and have been mathematically shown to obey the temporal Snell's law in section 2.2. The intensity of the plane waves output by the source follow a Gaussian distribution in time. A detector monitors and records the electric and magnetic field magnitudes across time. The time-dependent refractive index material is the substrate which the plane waves move through and imposes the time-varying refractive index causing time-refraction. Throughout this project pump and probe "duration" is the full-width at half-maximum of the respective pulse (for the error function introduced in section 3.4.1 this is the full-width half-maximum of the derivative i.e. a Gaussian).

3.3.1 Boundary Conditions

Simulations must be confined to a finite region of space and time in order for a finite computer to run them in a finite amount of time. To achieve this finite simulation region, boundary conditions at the spatial boundaries are required. In this project, light is propagated from a plane wave source on the left of the simulation region to a detector on the right of the simulation region, as shown in figure 2.
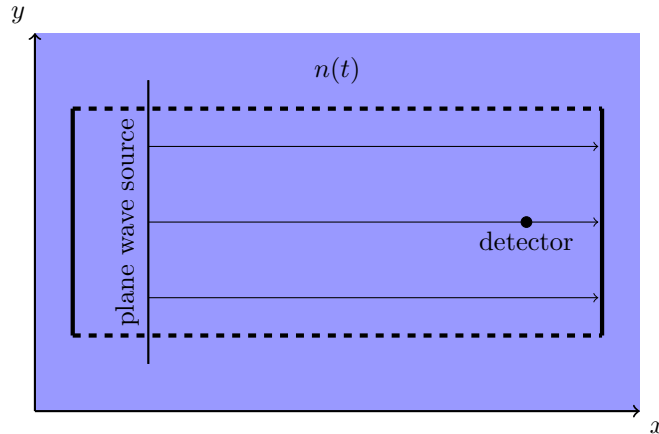

Figure 2: A diagram showing the simulation set up used throughout this project. A source and detector are shown within solid and dashed boundaries. Arrows indicate wavefronts travelling from the source to the detector. The blue shaded region indicates the region subject to a dynamic refractive index $n(t)$.

Figure 2 shows the boundaries confining the simulation region around the source and detector.

The "x-boundaries", indicated by the thick solid lines, are "PML" boundaries which aim to entirely absorb incident light without reflections [27]. The "y-boundaries", indicated by the thick dashed lines, are periodic boundaries. When light is incident on the upper periodic boundary it is re-emitted with the same properties at the lower periodic boundary and vice versa [28]. This has the effect of making the simulation behave identically as it would if it was repeating periodically to infinity in the vertical direction, with an infinite time-dependent material and an infinite plane wave source. Furthermore, the perfectly absorbant x-boundaries mean that the plane wave and detector behave as though they are a discrete distance apart within a material that extends to infinity along the x-axis. Finally, the simulation is performed in only two spatial dimensions, x and y. This means that the electric and magnetic fields, as well as the time-dependent material, are assumed to be homogeneous in the z-direction. This is identical to assuming that the plane wave source and material are infinite in the z-direction. These facts combine to imply that the simulated wavefronts behave as planes, infinite in the y and z directions, and the detector's output is independent of its y and z position.

3.4 Modelling Time-Dependent Refractive Index

In this project two of the physical methods for achieving a time-dependent refractive index considered in section 2.3 are modelled.

3.4.1 Free Carrier Dispersion - Error Function Δn

In optically induced free carrier dispersion (section 2.3.2), it can be assumed that the rate of carrier excitation is directly proportional to the intensity of the pump pulse. This implies that the total number of excited free carriers is given by the integral of the intensity of the light source with respect to time. If the intensity (I) of the pump pulse is defined by a Gaussian in time then the free carrier density (ρ) is proportional to an error function (an integrated Gaussian function). The free carrier density is proportional to Δn, according to equation 11. This is summarised in equation 20 ($t = 0$ is the start of the simulation, t' is an arbitrary time in the simulation, gauss is a Gaussian function and erf is an error function):

$$
\begin{aligned}
I &= \mathrm{gauss}(t - t_0) \\
\rho &\propto \int_0^{t'} \mathrm{gauss}(t - t_0) dt \\
\rho &\propto \mathrm{erf}(t') \\
\Delta n &\propto \mathrm{erf}(t')
\end{aligned}
\tag{20}
$$

As mentioned in section 2.3.2, the free carriers decay on the nanosecond order while they can be excited on the picosecond order. Therefore, the decay of free carriers is ignored in this model. A Lumerical FDTD material with a refractive index following a user-defined error function was used to model optically induced free carrier dispersion. Figure 3 shows the Δn of these materials.
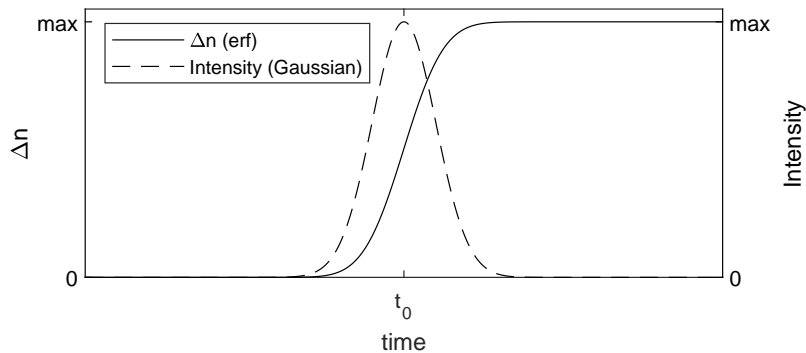

Figure 3: A plot of the intensity against time of a Gaussian pump pulse and the modelled resultant free carrier induced Δn.

3.4.2 The Optical Kerr Effect - Gaussian Δn

Equation 13 shows that $\Delta n \propto I$, where I is the intensity of light for a material susceptible to the optical Kerr effect (section 2.3.3). Therefore, if a Gaussian pump-probe is assumed, Δn can also be modelled by a Gaussian function ($\Delta n = \text{gauss}(t)$). A Lumerical FDTD material with a refractive index following a user-defined Gaussian was used to model the optical Kerr effect.

3.5 Normalisation

To make the results of the simulations in this project as generalisable as possible the significant factors in the project were normalised against a normalising constant a. a was selected to be an arbitrary value with units of spatial length. This has the benefit of being able to express spatial lengths in units of a, durations of time in units of a/c, and frequencies in units of c/a (where c is the speed of light in vacuum). As Maxwell's equations are scale-invariant [29] (i.e. $\mathbf{E}(\mathbf{r}, \mathbf{t})$ and $\mathbf{E}(\alpha\mathbf{r}, \alpha t)$ have the same form for any positive real α). Therefore, when a simulation is run with parameters normalised to a specific value of a, it is also solved for all positive real values of a. The normalised quantities in this project are shown in equations 21-25:

$$f = \frac{c}{a} \tag{21}$$

$$\Delta f = \Delta_f a \tag{22}$$

$$\Delta t_p = p(a/c) \tag{23}$$

$$x_{\text{span}} = x_c a \tag{24}$$

$$y_{\text{span}} = y_c a \tag{25}$$

In equations 21-25, f is the central frequency of the probe source, Δf is the full-width half-maximum of the frequencies output by the probe source, Δt_p is the full-width half-maximum in time of the probe source, x_{span} is the distance from the probe source to the detector and y_{span} is the distance from one y-boundary to the other. Δ_f, p, x_c and y_c are all proportionality constants used to adjust the variables relative to a.

Throughout this project a was set to 1µm but results can be generalised to any positive real length a. Throughout the entire project y_{span} was set to $5a$.

3.6 Simulation Resolution and Convergence

3.6.1 Mesh Resolution

According to the central difference equation (equation 17), smaller Δx, Δy, Δz and Δt will improve the accuracy of approximations. As this mesh spacing is decreased the simulations are expected to converge on analytical solutions [30]. As all simulations in this project are performed in two spatial dimensions, a grid spacing variable, hereafter "mesh resolution" (δ), is defined such that $\delta = \Delta x = \Delta y$. In electromagnetic finite-difference time-domain simulations with two spatial dimensions the time step (Δt) must be set such that $\Delta t < \delta/(\sqrt{2}c)$. This is known as the "Courant condition" [31] and throughout this project Δt is defined such that $\Delta t = 0.99\delta/(\sqrt{2}c)$.

When applying the finite-difference time-domain there is a constant trade-off between simulation accuracy and computing time and memory available. A smaller δ results in a greater simulation accuracy but at the cost of more calculations for the computer to process (i.e. the simulation takes longer to run) and more data to store for a given spatial and temporal simulation region.

3.6.2 Relative Mesh Resolution

The accuracy of the simulation depends not only on δ, but also on the wavelength (λ) of the electromagnetic waves within the simulation. δ must be a small fraction of λ and the higher the ratio λ/δ, the more accurate the simulation. Furthermore, the frequency-time ratio $(1/f)/(\Delta t)$ must also be considered in the same manner. This is known as numerical dispersion [32] (different

wavelengths are simulated with different accuracies). Numerical dispersion poses a problem when a simulation contains multiple refractive indices, either in time or space. The refractive index boundary changes λ (spatial) or f (temporal) and hence changes the accuracy of the simulation. All mesh resolutions must therefore be set according to the worst-case scenario, that is, light travelling through the material with the highest refractive index. A relative mesh resolution equation (shown in equation 26) is used to set δ, where $n_{\max}$ is the maximum refractive index:

$$\delta_r = n_{\max}\delta = \Delta x = \Delta y = 0.99\Delta t\sqrt{2}c \tag{26}$$

Hence the higher $n_{\max}$, the smaller the required δ for a desired δ_r. As $1/n_{\max} \propto \Delta x \propto \Delta y \propto \Delta t$, a two-fold increase in $n_{\max}$ results in a eight-fold (2^3) increase in the number of calculations required and hence an eight-fold increase in the time and memory required to run the simulation. Practically, this means that an $n_{\max}$ of greater than 3 is impractical to simulate accurately. Throughout this project the highest n simulated is 3.

3.6.3 Convergence of the Simulated Speed of Light

A pump-probe simulation was run for different relative mesh resolutions in order to observe the convergence of the speed of light. Figure 4 shows the convergence of the simulated speed of light on the analytical value (c_0):
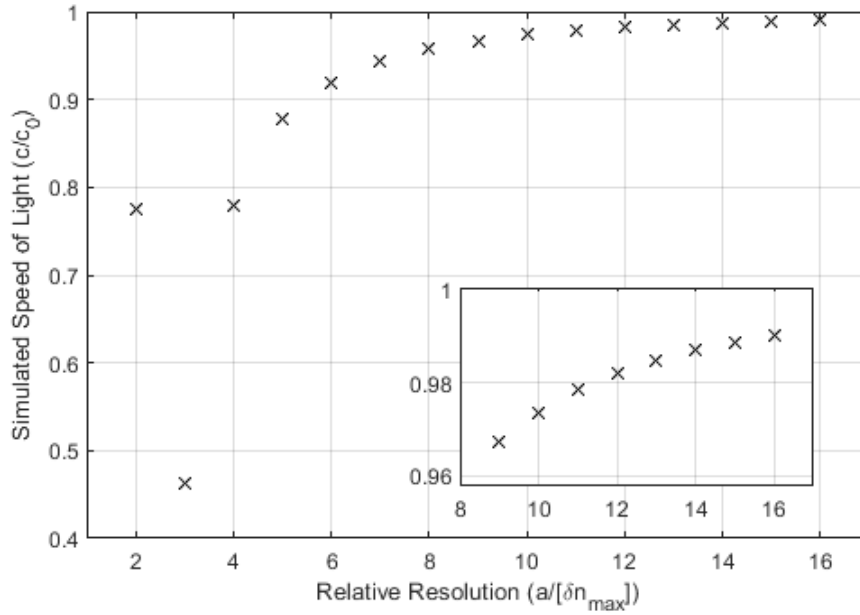

Figure 4: A plot of the simulated speed of light against the relative mesh resolution of the simulation.

Figure 4 shows that in order to achieve a simulation that propagates light at 99% of the analytical speed, a δ_r of $16a$ is required. To verify the relative mesh resolution equation (equation 26), the refractive index of the simulation medium was varied. It was found that for all refractive indices the convergence plots were identical ($\delta_r = 16 \implies c/(c_0/n) \approx 99\%$ for all tested n), implying that equation 26 is correct.

3.7 Pump-Probe Heat-Maps

Consider a detector within a material with a time-dependent refractive index defined by an error function. The error function increases n from n_1 to n_2 at a specific time defined by the pump-probe delay. To verify that the error function is in fact increasing n a pump-probe experiment

can be run at a highly positive pump-probe delay and a highly negative pump-probe delay. At a highly positive pump-probe delay, the error function will be triggered after the probe reaches the detector and the probe will be detected at time $n_1 x_{\mathrm{span}}/c$. At a highly negative pump-probe delay, the error function will be triggered before the probe is emitted and the probe will be detected at time $n_2 x_{\mathrm{span}}/c$. Intensity-time data from such simulations are shown in figure 5:
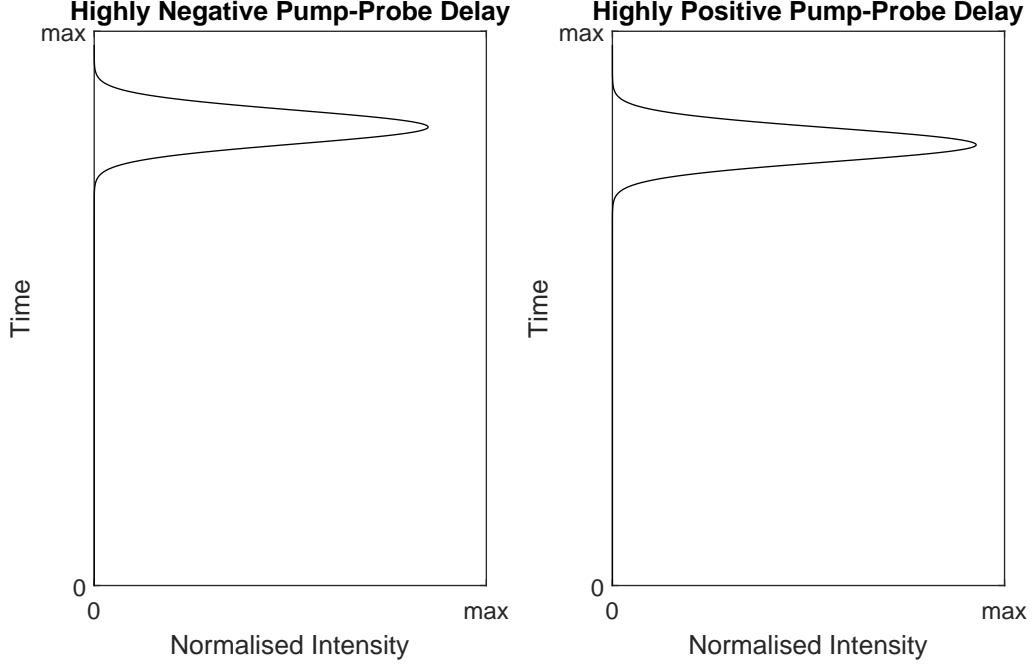

Figure 5: An example of time against intensity data from two pump-probe experiments with different pump-probe delays.

Figure 5 shows the delay in the arrival of light between two pump-probe delays. If the intensity-time plots from many different pump-probe delays needed to be shown then this method of plotting separately would be inefficient. Instead, the normalised intensity axis can be converted to a colour axis and resulting colour varying line can be used a "slice" in a heat-map. A heat-map containing the above data and many more simulations for pump-probes between the "highly negative" and "highly positive" pump-probe delays is shown in figure 6:
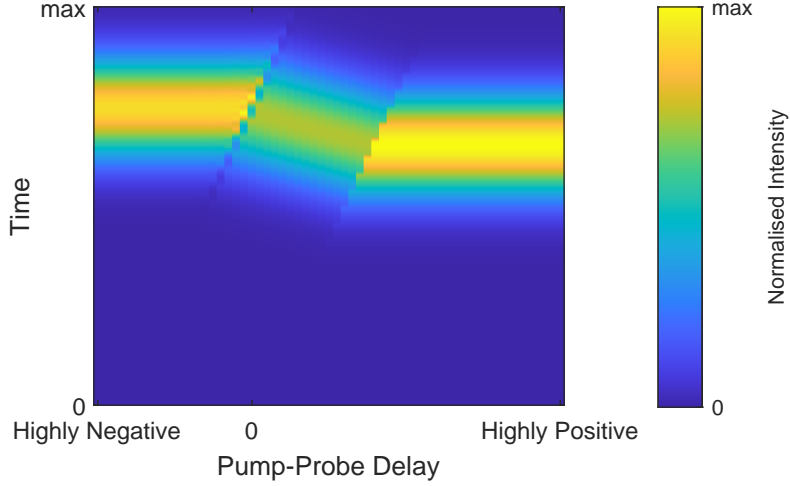
Figure 6: A heat-map showing time-intensity data against pump-probe delay. The figure shows data from a multitude of simulations as individual slices in a heat-map. The data shown in figure 5 correspond to the left-most and right-most slices of this heat-map respectively.

4   Results and Discussion - Error Function Δn

First, an error function defined (modelling optically induced free carrier dispersion) time-dependent refractive index material was explored.

4.1   Demonstrating Frequency Shift

A pump-probe simulation was created with the intention of observing a frequency shift due to time refraction. In order for a frequency shift to be observed the light must be subject to a change in n i.e. n_1 when the probe pulse is emitted must be different to n_2 when the probe pulse is detected. Consider a highly positive pump-probe delay i.e. Δn is excited long after the probe pulse had passed the detector. In this case no shift would be observed as n would have been stationary while the probe pulse was moving through the simulation. Alternatively, consider a highly negative pump-probe delay i.e. Δn is excited long before the probe pulse is emitted. Again, no shift would be observed because Δn would have plateaued before the probe was ever emitted. It is only when the pump-probe delay is such that the error function is excited while the probe pulse is between the source and detector that a frequency shift is expected.

A series of simulations were run with an $n_1 = 1$ and $\Delta n = 0.118$, giving $n_2 = 1.118$. A pump duration (error function duration) of $1a/c$, a probe duration of $25a/c$ and $x_{\mathrm{span}} = 75a$. The detector's intensity-time data is Fourier transformed to obtain frequency data.
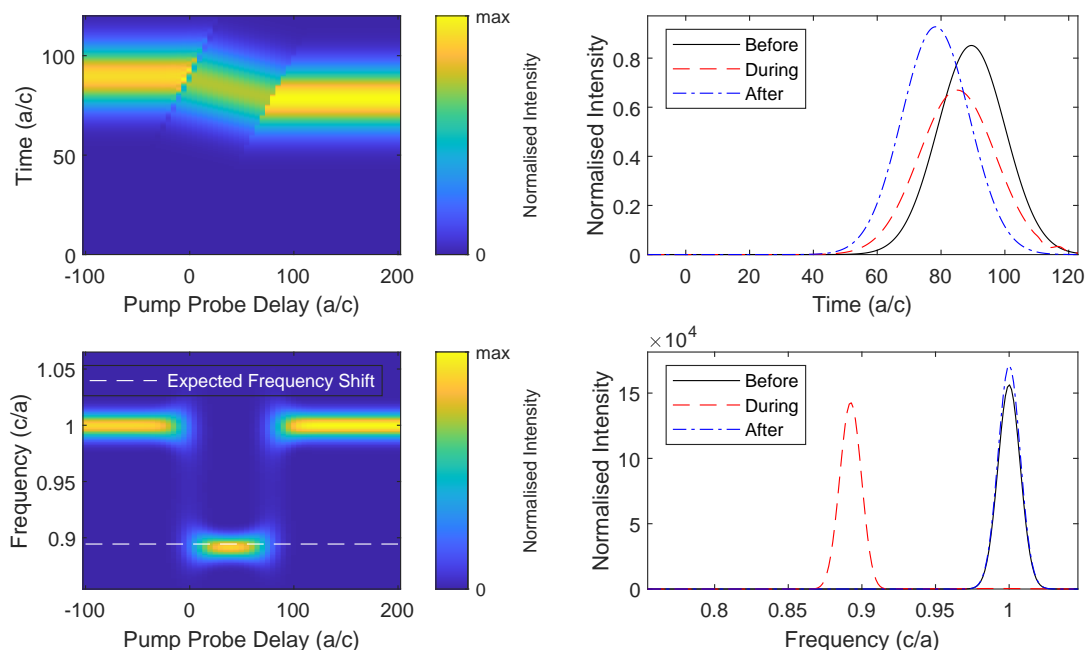
Figure 7: Data from a series of simulations with an error function defined time-dependent refractive index material with pump-probe delays between $-100a/c$ and $200a/c$. **Top left**: A heat-map showing the detected intensity as a function of time (since probe emission) against pump-probe delay. **Top right**: A plot showing the detected intensity against time of three select individual simulations at different pump-probe delays. "Before" corresponds to negative pump-probe delays, where Δn is excited before the probe pulse. "During" corresponds to low positive pump-probe delays where Δn is excited while the probe pulse is between the source and detector. "After" corresponds to high positive pump-probe delays where Δn is excited after the probe pulse has passed the detector. **Bottom left**: A heat-map showing the Fourier-transformed frequency data from the detector against pump-probe delay. An expected frequency shift using the temporal Snell's Law (equation 9) is shown. **Bottom right**: A plot showing the Fourier transformed frequency data of three select individual simulations. "Before", "During" and "After" labeling is the same as in the top right plot.

Figure 7 shows, as expected, time-refraction for pump-probe delays between about 0 and $75a/c$. The top left heat-map in figure 7 shows the probe pulses arriving at the detector at a later time for negative pump-probe delays than for positive pump-probe delays. This is expected as the refractive index that the pulse travels through is higher after Δn has taken place. The bottom left heat-map in figure 7 shows a frequency shift approximately matching the frequency shift predicted by the temporal Snell's law. This shift can also be seen in the bottom right plot in figure 7. At negative and high positive pump-probe delays no frequency shift is observed as the probe pulse experiences no Δn. A difference in intensity for all three detected pulses are shown in the top right and bottom right plots in figure 7. A change in intensity of the time-refracted pulse can be explained by the "peloton effect[1]". The discrepancy between the intensities of the "Before" and "After" pulses can not be explained by physical processes. This is assumed to be an effect of decreased simulation accuracy as the wavelength of light is decreased in the higher n material.

---

[1]Imagine a group of photons spread slightly in space and travelling at speed c_1. If the group of photons are simultaneously slowed to c_2 by time-refraction, the rate at which the number of photons pass a point in space will be slowed. This change in rate of photons is observed as a change in detected intensity such that $c_2/c_1 = I_2/I_1$.

4.2 Frequency Shift Convergence

The convergence of the observed frequency shift in finite-difference time-domain simulations on the temporal Snell's law can be tested. Simulations with a probe duration of $5a/c$, a pump duration of $1a/c$, $x_{\text{span}} = 50a$, a pump-probe delay of $15a/c$ (to ensure probe was subject to Δn), $n_1 = 1$ and $\Delta n = 2$ giving $n_2 = 3$ were run for a range of δ_r. The resulting convergence is shown in figure 8:
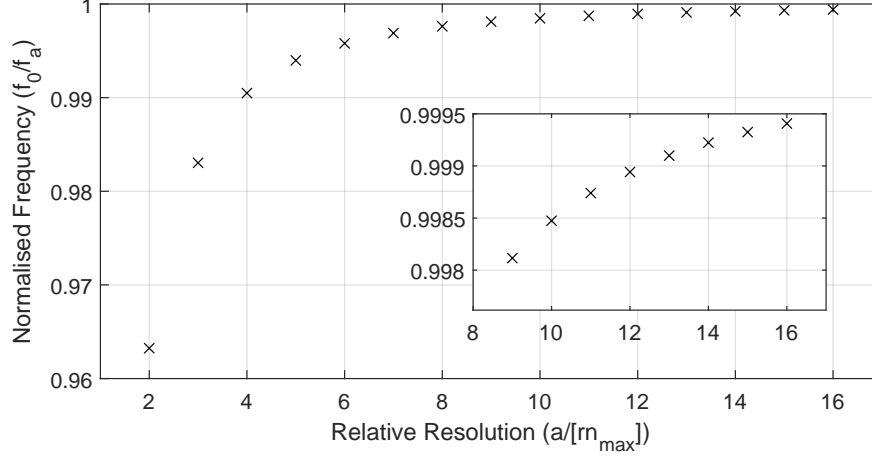

Figure 8: A plot of detected frequency (f_0) normalised against expected analytical frequency f_a against relative resolution.

Figure 8 shows the detected frequency (f_0) converging on an analytical solution for frequency shift (f_a) calculated with the temporal Snell's law. This increases confidence in the validity of the finite-difference time-domain method for simulating time-refraction. The plot shows that a frequency shift with greater than 99.9% accuracy can be achieved with a relative resolution of $13a$, furthermore an accuracy of approximately 99.85% can be achieved with a relative resolution of $10a$. Hereafter, simulations were run with a relative resolution of $10a$ to visually confirm phenomena and a relative resolution of $13a$ was used if numerical analysis was to be performed on the resultant data.

4.3 Negative Δn

Δn can be made negative in order to observe a positive frequency shift (blue-shift). Physically this would mean depleting free carriers from a material. Figure 9 shows a positive frequency shift achieved with a probe pulse duration of $20a/c$, a pump duration of $1a/c$, $x_{\text{span}} = 75a/c$, $n_1 = 2$ and $\Delta n = -0.775$ giving $n_2 = 1.225$ for a range of pump-probe delays.
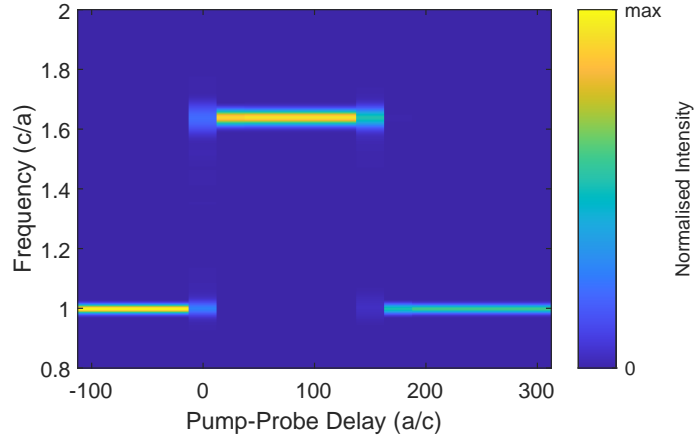
Figure 9: Detected frequency data against pump-probe delay for a pump-probe experiment performed with a negative Δn.

Figure 9 shows, as expected, a blue shift. The exact relationship between Δn and observed frequency shift is explored in section 4.6.

4.4 Varying Simulation Length ($x_{\mathbf{span}}$)

The effect of increasing and decreasing x_{span} was explored. Simulations with a probe pulse duration of $20a/c$, a pump duration of $1a/c$, $n_1 = 2$ and $\Delta n = -0.775$ giving $n_2 = 1.225$ were run while varying pump-probe delay and simulation length. The resulting frequency data is shown in figure 10. As the detector is being extended further from the source the range of pump-probe delays which result in a Δn being experienced by the probe is expected to increase because the probe spends longer travelling from the source to the detector.
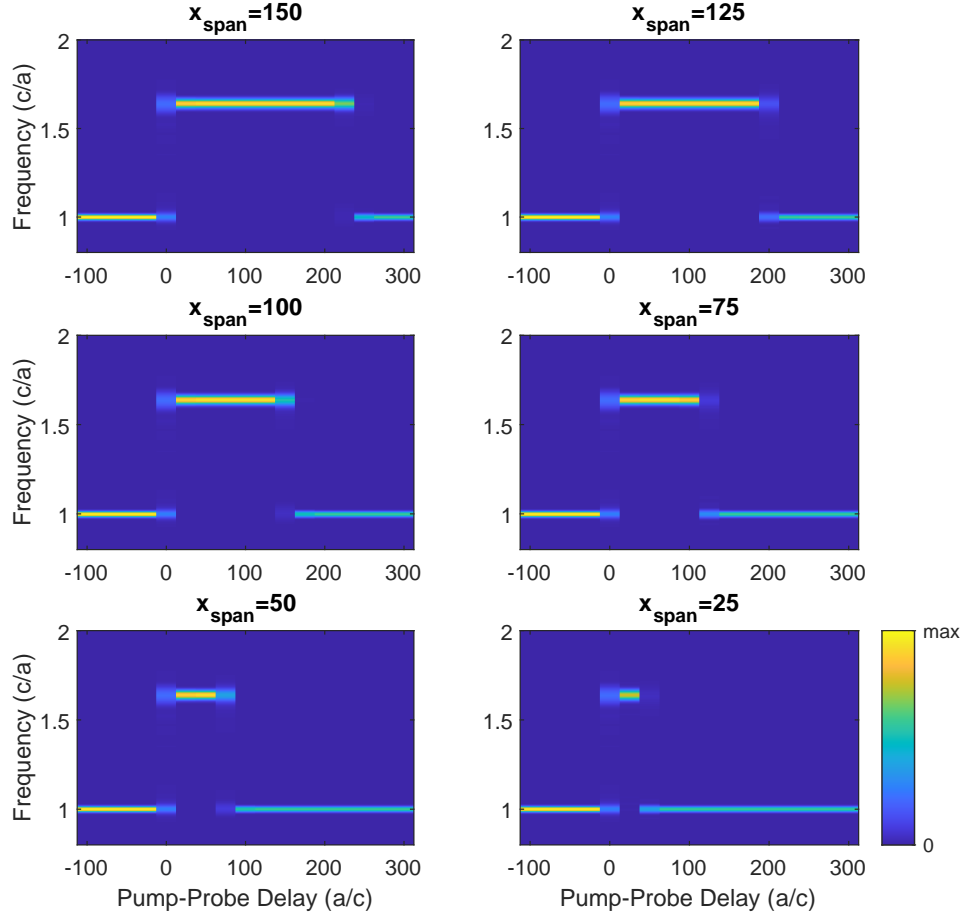
Figure 10: Plots of detected frequency against pump-probe delay for different simulation lengths. Plot titles label the x_{span} of each simulation.

Figure 10 shows, as expected, an increase in the range of pump-probe delays which result in time-refraction. Assuming that the pump duration is negligibly short in comparison to nx_{span}/c (the time the pump takes to travel from the source to the detector), the range of pump-probe delays which result in observed time-refraction are given by nx_{span}/c.

4.5 Varying Pump Duration

Another interesting variable to change is the pump duration (error function duration). Thus far a very short $(1a/c)$ pump duration has been used. A longer pump duration would be expected to give a wider range of pump-probe delays which result in time-refraction. This is because even if a pump pulse is centred at a time when the probe has passed the detector or has not yet been emitted, the probe pulse may still be subject to the "tails" of the error function. As the probe would only be subject to the "tails" of the error function a smaller Δn and therefore a smaller Δf is expected. Furthermore, if the pump duration is longer than the amount of time the probe requires to move from the source to the detector then it will be impossible for the probe to experience the full Δn and therefore a smaller Δf is expected to be observed across all pump-probe delays. The same experiment as in section 4.4 (varying simulation length) was performed except the pump duration was changed from $1a/c$ to $100a/c$. The frequency data is shown in figure 11:
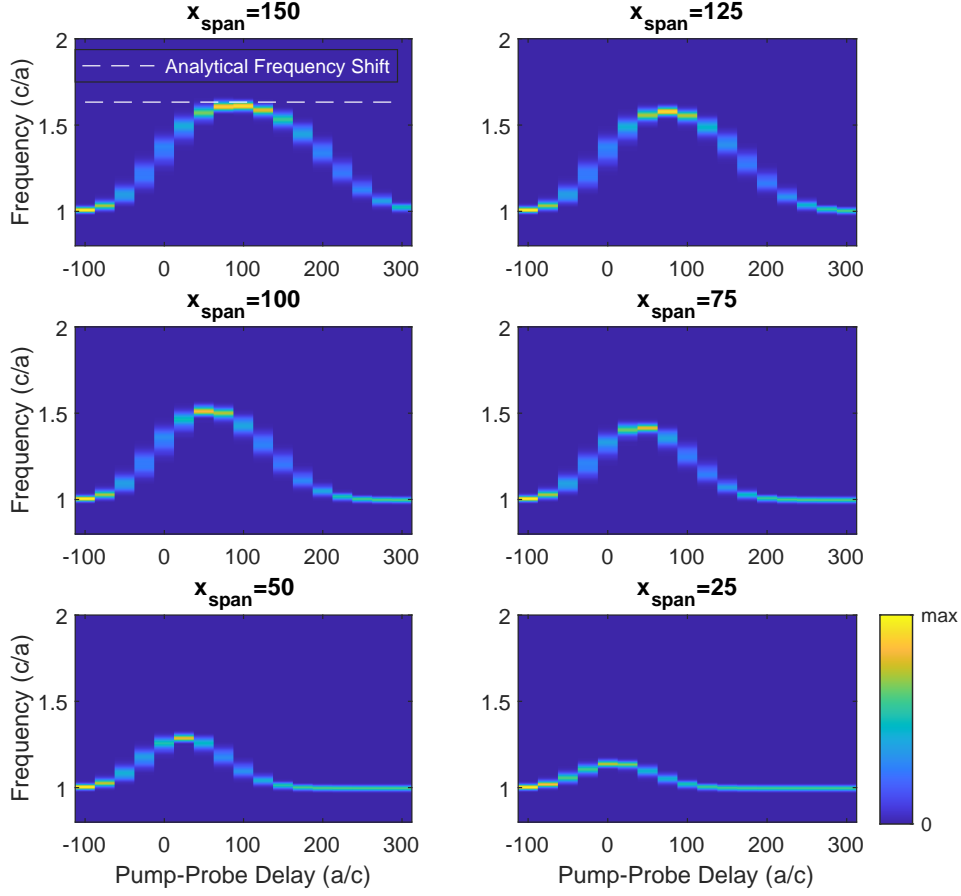
Figure 11: Plots of detected frequency against pump-probe delay for different simulation lengths with a long pump pulse duration. Plot titles label the x_{span} of each simulation.

Figure 11 shows that as expected, the range of pump-probe delays for which time-refraction is observed is extended when the pump duration is extended from $1a/c$ to $100a/c$. Furthermore, the expected reduction in frequency shift as x_{span} is reduced is also observed.

4.6   Testing the Temporal Snell's Law

Finally, the temporal Snell's law derived in section 2.2 was tested against the error function defined time-dependent refractive index simulations. To ensure that the probe pulse was subject to as much of the error function as possible (as explained in section 4.5), a small pump pulse duration was used ($1a/c$) in conjunction with a comparatively high x_{span} ($40a$). To ensure greater than 99.9% converged frequency shift accuracy (section 4.2) a relative mesh resolution of $13a$ was used. A probe duration of $5a/c$ was used and a pump-probe delay of $15a/c$ was used. As the probe pulse has a full-width half-maximum of $5a/c$ and the pump-probe delay is $15a/c$, it can be calculated that far greater than 99.99% of the probe pulse has been emitted when the pump pulse is excited. Such simulations were run with $n_1 = 2$ and a range of Δn from -1 to +1. This gives a $\Delta n/n$ of $\pm 100\%$, while not causing n_{max} to become too large to simulate accurately (section 3.6). Once the frequency data of the time-refracted probe pulse had been recorded a Gaussian distribution was fitted to its spectrum to find the position of its maxima and hence the resultant frequency shift. Figure 12 shows the resultant frequency shifts:
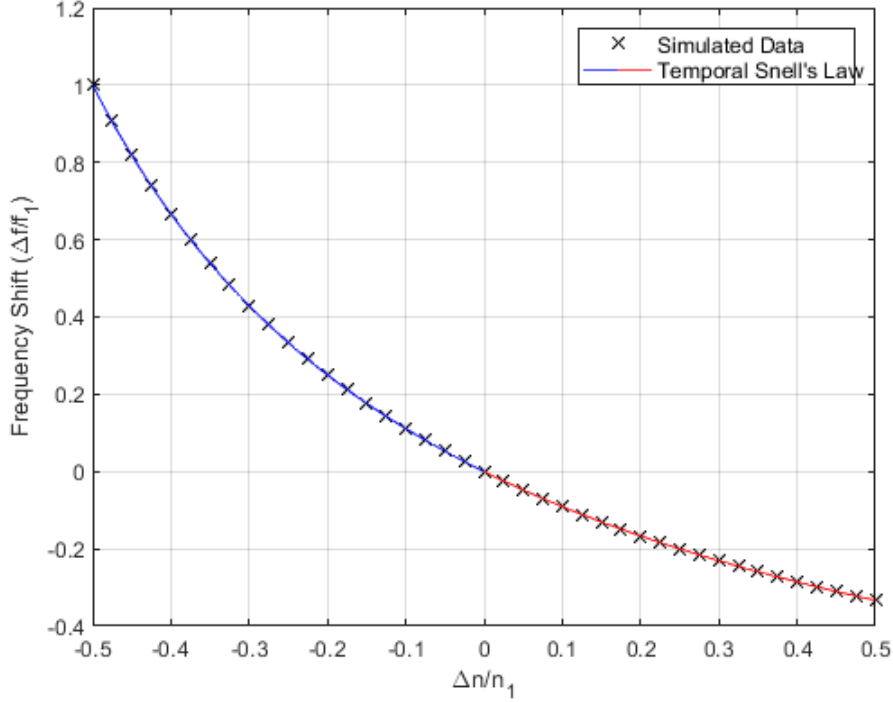
Figure 12: A plot of observed frequency shift against change in index when simulating a time-dependent material defined by an error function. Frequency shift is plotted as a fraction of the original unperturbed probe frequency (f_1) and change in index is plotted as a fraction of the original unperturbed refractive index (n_1). The expected blue and red shift from the temporal Snell's law is also plotted.

Figure 12 shows a very good agreement between the simulated frequency shifts and the analytical predictions from the temporal Snell's law. Figure 12 shows that the frequency shift is a nonlinear function of Δn. This is to be expected as the temporal Snell's law takes the form of equation 27:

$$n_1 f_1 = n_2 f_2 \implies \frac{\Delta f}{f_1} = \frac{n_1 f_1}{n_1 + \Delta n} - 1 \tag{27}$$

The temporal Snell's law can be linearised by taking the reciprocal of the shifted frequency ($1/f_2$) as shown in equation 28:

$$n_1 f_1 = n_2 f_2 \implies \frac{1}{f_2} = \frac{\Delta n}{n_1 f_1} + \frac{1}{f_1} \tag{28}$$

A straight line can be fitted to the $1/f_2$ against Δn data. As $f_1 = 1$ and $n_1 = 2$, the line of best fit is expected to be $f_2 = 0.5\Delta n + 1$ according to equation 28. The resulting fit is shown in figure 13:
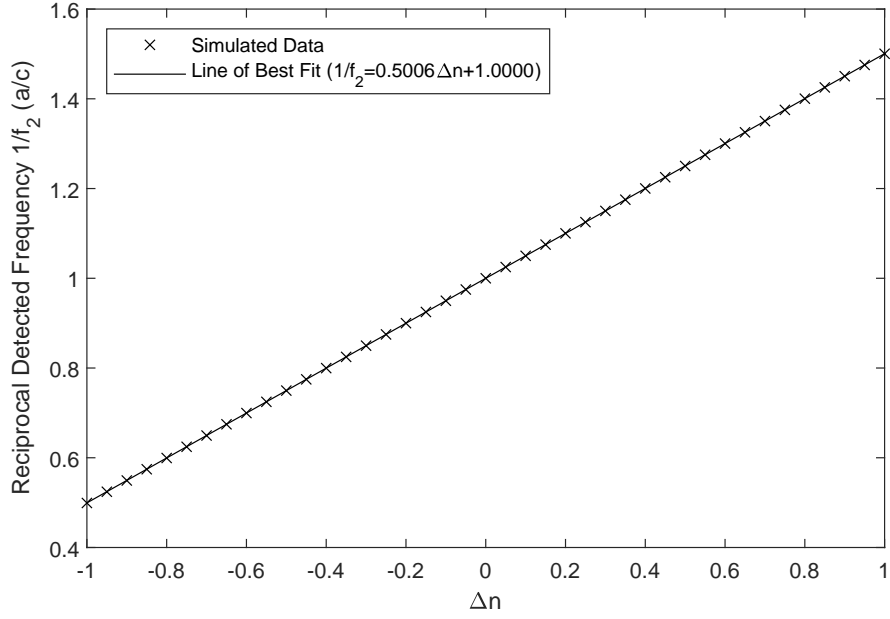
Figure 13: A plot of detected frequency (f_2) against change in refractive index (Δn). A line is fitted to the data with gradient 0.5006 ± 0.0001 and intercept 1 ± 0.0001 with a 95% confidence level.

The linear fit agrees with the analytical Snell's law prediction to within 0.2% in gradient and 0.01% in intercept. The fact that the analytical Snell's law falls outside of the gradient's 95% confidence interval (0.5 is not within 0.5006 ± 0.0001) suggests that there is some systematic error in the simulations likely caused by incomplete frequency shift convergence shown in section 4.2. This source of systematic error would lead to "smaller than analytical" maximum frequency shifts being detected which agrees with the "smaller than analytical" gradient found. The simulation results can be said to agree with the temporal Snell's law to better than 99.8%.

5 Results and Discussion - Gaussian Function Δn

A material with a refractive index defined by a Gaussian distribution (modelling the optical Kerr effect) in time was also explored.

5.1 Demonstrating Frequency Shift

Observing time-refraction due to a Gaussian Δn presents a problem not present when using an error function defined Δn. The full Δn caused by a Gaussian function, from long before its central time (t_0) to long after t_0 is zero. Hence, if the probe pulse is subjected to the full Gaussian the probe will be blue-shifted and then red-shifted back to its original frequency i.e. the probe experiences a net Δn of 0 and a net frequency shift of 0. It will still be evident from the detected data that the light was subject to a change in Δn because the time at which the light arrives at the detector will have changed. In order to observe a frequency shift the probe pulse must be subject to only part of the Gaussian such that it experiences a net $\Delta n \neq 0$. This $\Delta n \neq 0$ is achieved by adjusting the pump-probe delay.

Once again, if Δn is triggered long before or long after (highly negative or highly positive pump-probe delays) the probe is emitted, no time-refraction will be observed. Furthermore the probe pulse will be subject to a positive or negative Δn, depending on the pump-probe delay. Consider a Gaussian index change adding a peak Δn of 1 to an n_1 of 1. If the light is subjected to a change from the base of the Gaussian to the peak of the Gaussian then the light will have been subject to a change in index from $n_1 = 1$ to $n_2 = 2$ and hence will experience a blue-shift.

22

Conversely, if the probe pulse is emitted while the Gaussian is at its peak, the probe will be subject to a change of index from $n_1 = 2$ to $n_2 = 1$ and hence will experience a red-shift.

A series of pump-probe experiments were run across a range of pump-probe delays. An x_{span} of $20a$, a probe pulse duration of $5a/c$, a pump pulse duration (Gaussian Δn) of $20a/c$, an n_1 of 2 and a Δn of 0.121 giving an n_2 of 2.121 was used. Knowing $n_1 = 2$ and $n_2 = 2.121$, the maximum blue ($n_2 \to n_1$) and red ($n_1 \to n_2$) shifts were predicted. Simulations were run with a relative mesh resolution of 10. The time-intensity and frequency-intensity data against pump-probe delay is shown in figure 14:
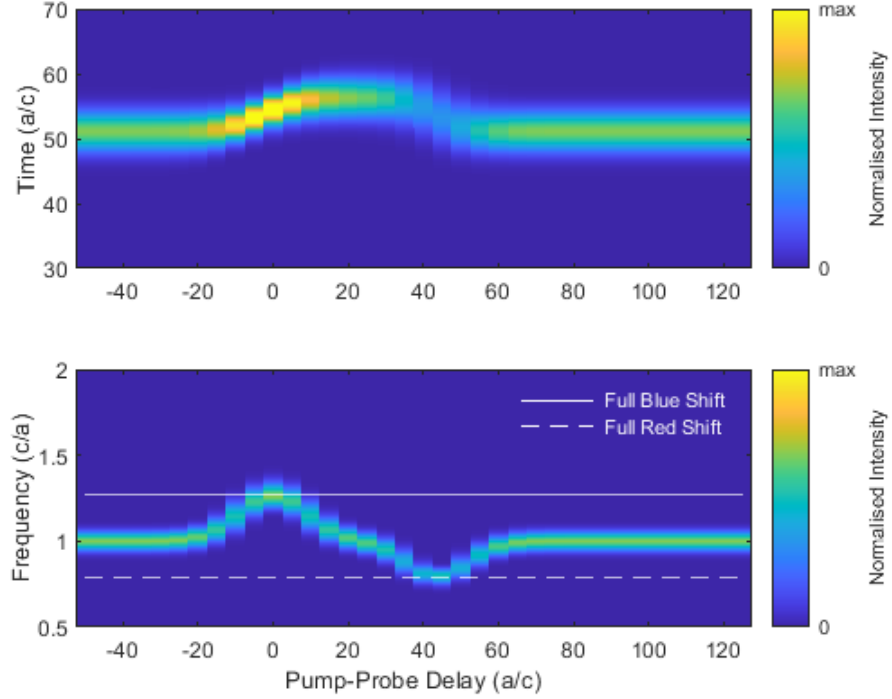

Figure 14: Heat-maps from a series of simulations with a range of pump-probe delays showing time-refraction due to a Gaussian defined change in refractive index. **Top**: Detected light intensity against time for a range of pump-probe delays. **Bottom**: Fourier transformed frequency intensity against pump-probe delay.

Figure 14 shows the expected variation in frequency shifts. For low pump-probe delays (-20 to $20a/c$), the probe is only affected by the "down slope" of the Gaussian i.e. $n_2 \to n_1$ and a blue shift is observed as expected. The maximum blue shift observed agrees well with the analytically predicted "full blue shift". For intermediate pump-probe delays (approximately $20a/c$), the probe is affected by both the "up slope" and the "down slope" of the Gaussian ($n_1 \to n_1$) and no frequency shift is observed. It can be seen that the light has still been subject to a changing refractive index however because the time-intensity heat-map shows the pulse arriving later. At high pump-probe delays (20 to $60a/c$), the probe is only affected by the "up slope" of the Gaussian i.e. $n_1 \to n_2$ and a red shift is observed as expected. The maximum red shift observed also agrees well with the analytically predicted "full red shift". At extreme positive and negative pump-probe delays no frequency shift is observed and no delay in the detection of the probe pulse is observed. This remains the same as in the error function defined material. Just as in the error function defined material, the "peloton effect" can be seen in the variation in the peak intensities in the time-intensity heat-map. The heat-map shows that as the light is subject to $n_2 \to n_1$ (pump-probe delays of -20 to $20a/c$) the intensity of the light

detected is increased because the pulse is sped up within the material. Alternatively, when the light is subject to $n_1 \to n_2$ (pump-probe delays of 20 to $60a/c$) the intensity of the light detected is decreased because the pulse is slowed within the material.

5.2 Negative Δn

As in section 4.3, a Gaussian with a negative amplitude, giving negative Δn, can also be modelled. It is less physically consistent with the optical Kerr effect but could be conceptualised as the momentary de-illumination of a material i.e. the momentary absence of the optical Kerr effect. The same simulations as in section 5.1 were run with the same parameters except Δn was set to -0.775 giving the same n_1 of 2 but a new n_2 of 1.225. The resultant time-intensity and frequency-intensity data against pump-probe delay is shown in figure 15:
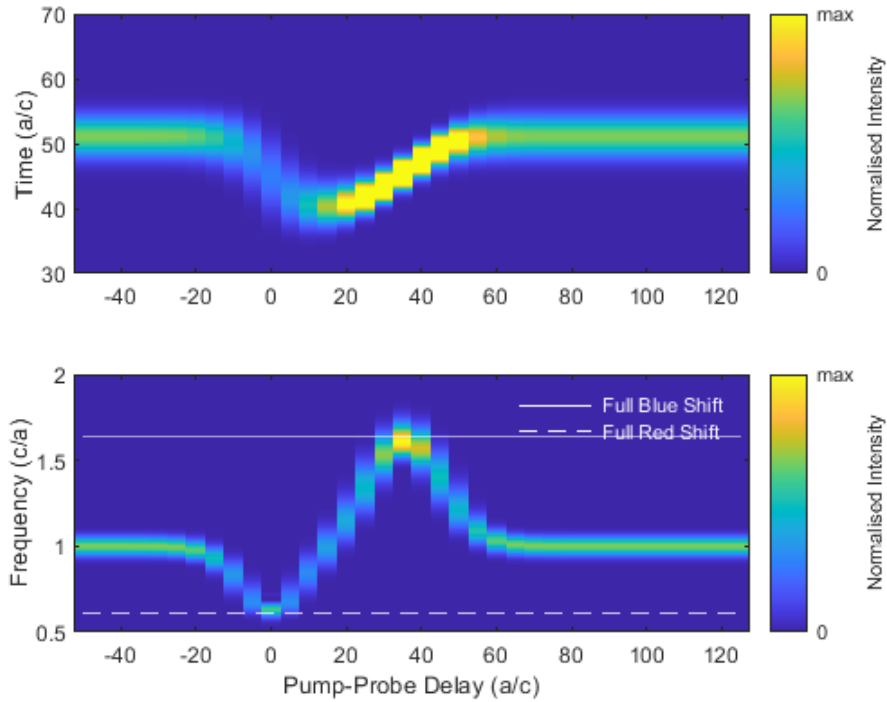

Figure 15: Heat-maps from a series of simulations with a range of pump-probe delays showing time-refraction due to a Gaussian defined change in refractive index. **Top**: Detected light intensity against time for a range of pump-probe delays. **Bottom**: Fourier transformed frequency intensity against pump-probe delay.

Figure 15 shows very similar data to figure 14 (positive Δn), except the time delay and the frequency shift are mirrored along the unperturbed horizontal line at times of approximately $50a/c$ and frequencies of $1c/a$. This mirroring is expected because what was an "up slope" in refractive index for the positive Δn case is now a "down slope" in this negative Δn case and vice versa. Again, the temporal Snell's law's analytical predictions for "full blue shift" and "full red shift" can be seen to agree well with the simulation data.

5.3 Varying Simulation Length ($x_{\mathbf{span}}$)

Next, the effect of varying the distance from the source to the detector was explored. The same simulation set up with the same parameters as in section 5.1 was run for several different x_{span}. Figure 16 shows the simulation data from various different simulation lengths:
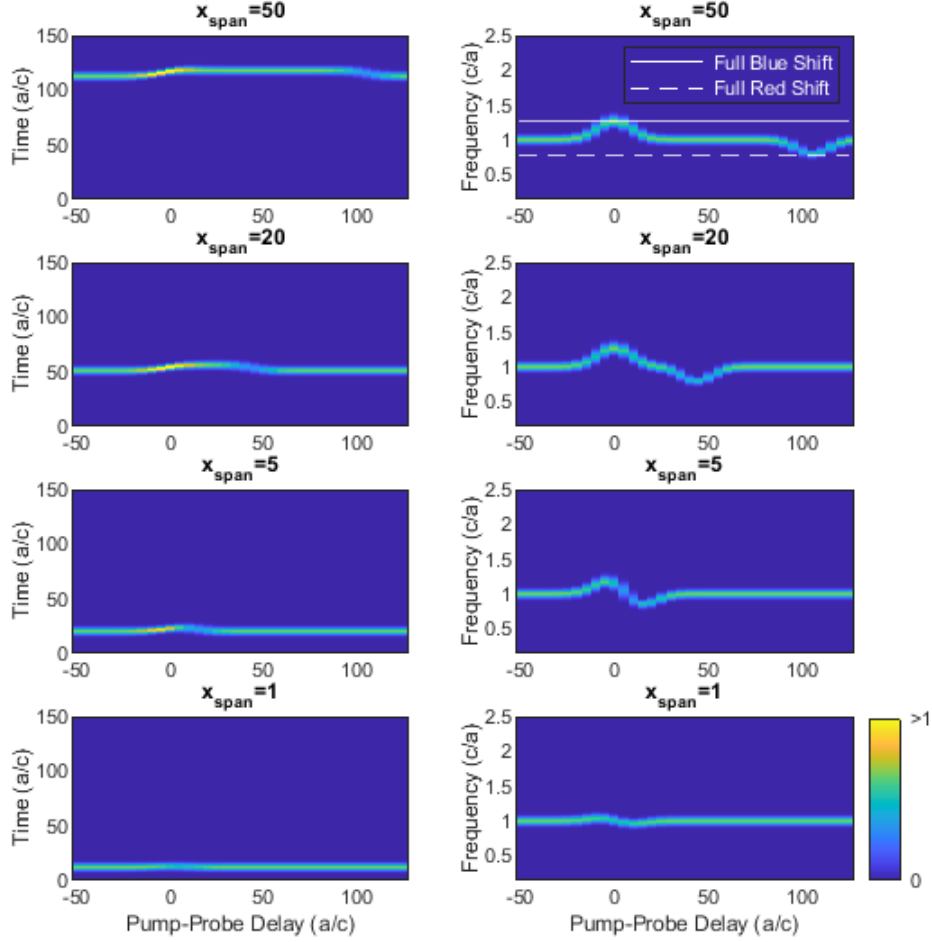
Figure 16: Heat-maps of detected intensity-time and frequency-time against pump-probe delay for a range of different simulation lengths. Analytical values from the temporal Snell's law for "full blue shift" and "full red shift" are shown.

Figure 16 shows that, as the distance from the source to the detector is varied, the frequency shifts observed are changed. As expected, at an x_{span} of $1a$, where the probe pulse passes from the source to the detector in a fraction of the duration of the Gaussian, a smaller maximum frequency shift is seen than at larger x_{span}. Furthermore, the range of pump-probe delays at which the probe pulse is subject to both red and blue shifts resulting in no overall frequency shift is increased as x_{span} is increased. This increase in null-shift range is most clear in the difference between $x_{\text{span}} = 20a$ and $x_{\text{span}} = 50a$.

5.4 Testing the Temporal Snell's Law

Finally, the effects of varying the Δn of the Gaussian and the resultant frequency shifts' agreement with the temporal Snell's law were explored. Heat-maps of the resultant pump-probe frequency data were made for different Δn (with otherwise identical parameters to section 5.1) to visually inspect the changes in frequency shift:
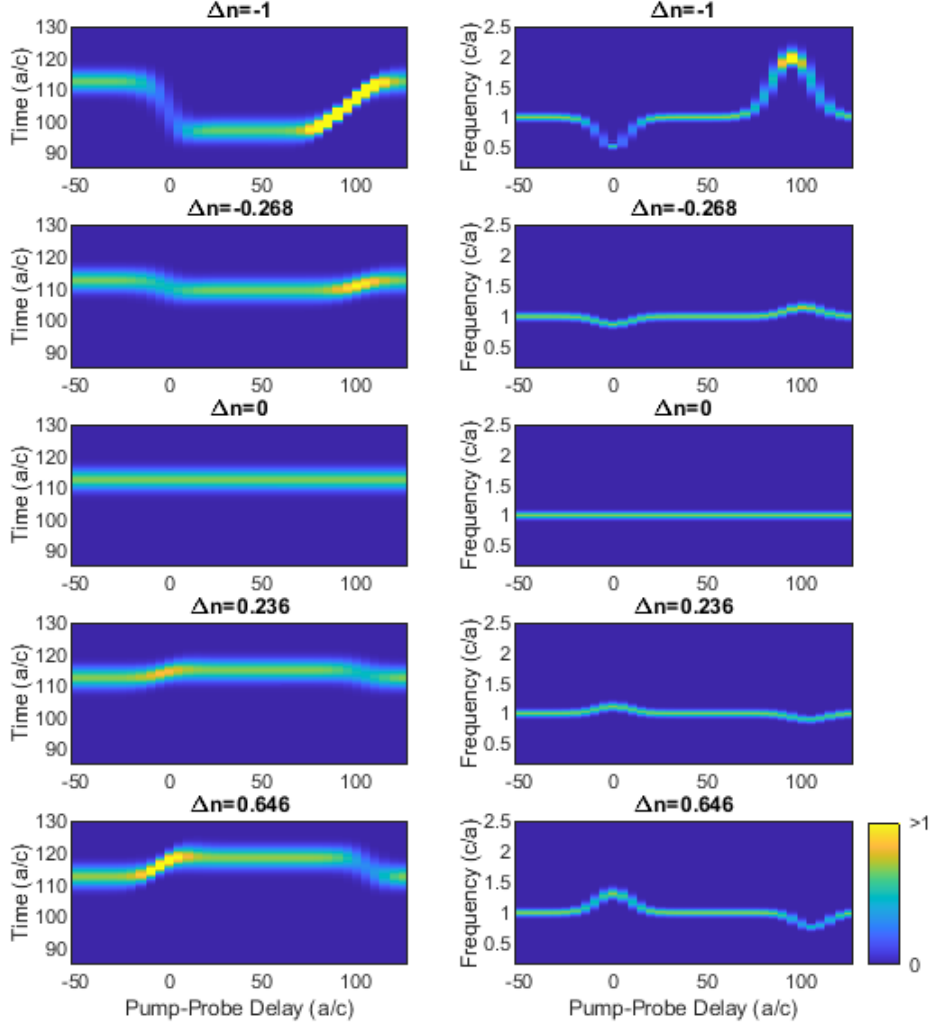
Figure 17: Heat-maps showing time-intensity (left) and frequency-intensity (right) against pump-probe delay data from a series of simulations for different Δn.

Figure 17 shows the time-intensity and frequency-intensity data for a range of Δn. As expected, the red and blue shifts are seen to get larger as $|\Delta n|$ is increased. To quantify the agreement between simulated data and the temporal Snell's law the maximum blue and red shifts from each simulation must be found. To quantify these extrema accurately, simulations with the exact pump-probes of the extrema must be run. A pump-probe delay of 0 gives one of the maxima corresponding to $n_2 \rightarrow n_1$ as shown in figure 17. On the other hand, the maxima from $n_1 \rightarrow n_2$ requires the pump pulse to reach its maximum at the exact same time that the probe pulse reaches the detector. The time at which the probe-pulse reaches the detector is dependent on Δn, the pump pulse (Gaussian) duration, the relative mesh resolution (section 3.6.3) and the pump-probe delay itself. Furthermore, the relative mesh resolution, which is set for the highest refractive index possible in the simulation, varies throughout the simulation as the refractive index of the material varies. For example, at a relative mesh resolution of 13 the simulated speed of light can vary from close to 100% of the analytical speed of light to closer to 98% of the analytical value when the maximum refractive index is present making analytically predicting the pump-probe delay corresponding to maximum shift very difficult. Therefore, when

finding maximum frequency shifts due to $n_1 \rightarrow n_2$, series of simulations such as the ones shown in figure 17, with relatively large steps in pump-probe delay, were used to find the approximate pump-probe delay of the maximum shift and then series of simulations with smaller steps in pump-probe delay were used to find a more precise pump-probe delay. The frequency shift data from these simulations are shown against $\Delta n/n_1$ in figure 18:
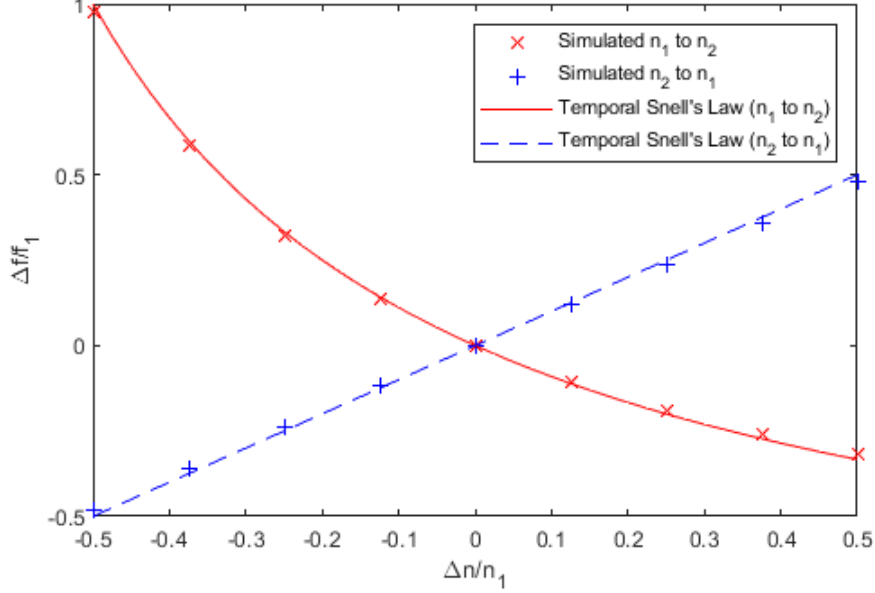

Figure 18: A plot of observed frequency shifts against change in index when simulating a time-dependent material defined by a Gaussian. Frequency shift is plotted as a fraction of the original unperturbed probe frequency (f_1) and change in index is plotted as a fraction of the original unperturbed refractive index (n_1). The expected blue and red shifts from the temporal Snell's law are also plotted.

It is unsurprising that the shift due to $n_1 \rightarrow n_2$ is identical to the plot in figure 12 as they are both showing a shift due to a change in index of $+\Delta n$ from n_1. $n_2 \rightarrow n_1$ on the other hand is a novel frequency shift which takes the form of a straight line against Δn. The $n_2 \rightarrow n_1$ shift is governed by the temporal Snell's law and can be expressed as equation 29:

$$f_2 n_1 = f_1(n_1 + \Delta n) \implies f_2 = f_1\left(1 + \frac{\Delta n}{n_1}\right) \tag{29}$$

In this case, where $n_1 = 2$ and $f_1 = 1$, the equation can be expressed as $f_2 = 0.5\Delta n + 1$.

Equation 28 ($1/f_2 = \Delta n/(n_1 f_1) + 1/f_1$) derived in section 4.6 governs $n_1 \rightarrow n_2$ shifts such that $1/f_2 = 0.5\Delta n + 1$. These two linear equations are fitted to and plotted in figure 19:
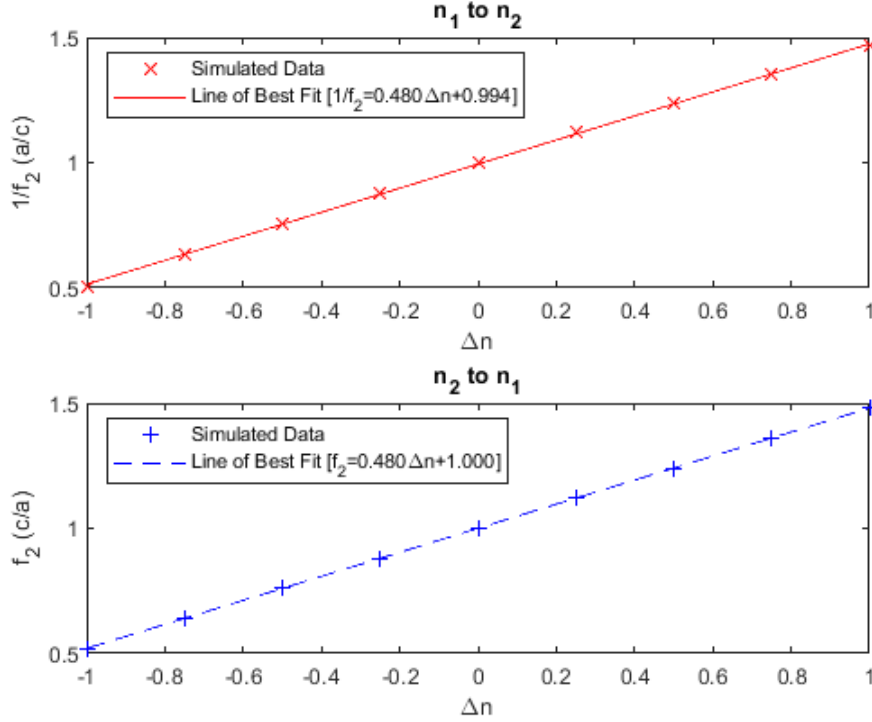
Figure 19: Two plots showing linearised frequency shifts from $n_1 \rightarrow n_2$ and $n_2 \rightarrow n_1$ and their lines of best fit. The $n_1 \rightarrow n_2$ is fit with a gradient of 0.480 ± 0.007 and an intercept of 0.994 ± 0.005. The $n_2 \rightarrow n_1$ is fit with a gradient of 0.480 ± 0.001 and an intercept of 1 ± 0.001 (all errors represent 95% confidence intervals).

The gradients of the linear fits are close to the expected gradients of 0.5 and the intercepts are close to the expected intercepts of 1. Both fitted gradients fall within 96% of the analytical gradient and both intercepts fall within 99.4% of the analytical intercept from the temporal Snell's law. Furthermore, the expected analytical gradients and intercepts fall outside of the 95% confidence intervals (except for the $n_2 \rightarrow n_1$ intercept). Again, this disagreement is likely because of systematic error caused by incomplete frequency shift convergence shown in section 4.2 as well as systematic error produced by being unable to find the exact pump-probe corresponding to maximum frequency shift (explained earlier in this section). Both of these sources of systematic error would lead to "smaller than analytical" maximum frequency shifts being detected which agrees with the "smaller than analytical" gradients found. The simulation results can be said to agree with the temporal Snell's law to better than 96%.

6   Conclusions

Two models for time-dependent refractive indices were modelled, an error function and a Gaussian function, and light was propagated through them with finite-difference time-domain simulated experiments. The requirements for achieving maximum frequency shift were determined through many pump-probe experiment simulations with different pump-probe delays. The effect of simulation length (distance from source to detector), change in refractive index and pump duration (for the error function only) on frequency shift investigated.

A temporal equivalent of Snell's law [1] was derived and was shown to agree with simulations to within 99.8% (error function) and 96% (Gaussian) of simulated frequency shifts. To the author's knowledge this is the first confirmation of the accuracy of the temporal Snell's law. This

agreement was shown for frequency shifts from +100% to -50% where prior frequency shifts had only been demonstrated for ±6% [2].

This project improves confidence in the validity of the temporal Snell's law as well as the validity and accuracy of using finite-difference time-domain simulations to investigate and model time-refraction and the resultant frequency shifts, particularly for high frequency shifts.

An interesting further investigation could involve re-running these simulations with the light confined in a resonant structure. This would enforce discrete modes on the light and would allow for adiabatic frequency conversion to be investigated.

References

[1] J. Mendonça and P. Shukla, "Time refraction and time reflection: two basic concepts", Physica Scripta **65**, 160 (2002).

[2] Y. Zhou, M. Z. Alam, M. Karimi, J. Upham, O. Reshef, C. Liu, A. E. Willner, and R. W. Boyd, "Broadband frequency translation through time refraction in an epsilon-near-zero material", Nature communications **11**, 1–7 (2020).

[3] J. Dias, C. Stenz, N. Lopes, X. Badiche, F. Blasco, A. Dos Santos, L. O. e Silva, A. Mysyrowicz, A. Antonetti, and J. Mendonça, "Experimental evidence of photon acceleration of ultrashort laser pulses in relativistic ionization fronts", Physical review letters **78**, 4773 (1997).

[4] G. Woan, *The cambridge handbook of physics formulas*, eng (Cambridge University Press, Cambridge, 2000), p. 152.

[5] J. Mendonça, "Time refraction in expanding plasma bubbles", New Journal of Physics **11**, 013029 (2009).

[6] N. Lopes, G. Figueira, J. Dias, L. Silva, J. Mendonça, P. Balcou, G. Rey, and C. Stenz, "Laser pulse frequency up-shifts by relativistic ionization fronts", EPL (Europhysics Letters) **66**, 371 (2004).

[7] G. T. Reed and A. P. Knights, *Silicon photonics: an introduction* (John Wiley & Sons, 2004), p. 101.

[8] M. Castellanos Muñoz, A. Y. Petrov, and M. Eich, "All-optical on-chip dynamic frequency conversion", Applied Physics Letters **101**, 141119 (2012).

[9] T. Kampfrath, D. M. Beggs, T. P. White, A. Melloni, T. F. Krauss, and L. Kuipers, "Ultrafast adiabatic manipulation of slow light in a photonic crystal", Physical Review A **81**, 043837 (2010).

[10] J. Upham, Y. Tanaka, T. Asano, and S. Noda, "On-the-fly wavelength conversion of photons by dynamic control of photonic waveguides", Applied physics express **3**, 062001 (2010).

[11] G. T. Reed and A. P. Knights, *Silicon photonics: an introduction* (John Wiley & Sons, 2004), pp. 73–74.

[12] R. W. Boyd and D. Prato, *Nonlinear optics*, eng (Elsevier Science & Technology, San Diego, 2008), pp. 207–210.

[13] R. W. Boyd and D. Prato, *Nonlinear optics*, eng (Elsevier Science & Technology, San Diego, 2008), pp. 1–2.

[14] G. P. Agrawal, P. Baldeck, and R. Alfano, "Temporal and spectral effects of cross-phase modulation on copropagating ultrashort pulses in optical fibers", Physical Review A **40**, 5063 (1989).

[15] J. Li, B.-E. Olsson, M. Karlsson, and P. A. Andrekson, "Otdm add-drop multiplexer based on xpm-induced wavelength shifting in highly nonlinear fiber", Journal of lightwave technology **23**, 2654 (2005).

[16] P. Mehta, N. Healy, T. Day, J. Badding, and A. Peacock, "Ultrafast wavelength conversion via cross-phase modulation in hydrogenated amorphous silicon optical fibers", Optics express **20**, 26110–26116 (2012).

[17] R. Dekker, A. Driessen, T. Wahlbrink, C. Moormann, J. Niehusmann, and M. Först, "Ultrafast kerr-induced all-optical wavelength conversion in silicon waveguides using 1.55 μm femtosecond pulses", Optics express **14**, 8336–8346 (2006).

[18] H. Suchowski, G. Porat, and A. Arie, "Adiabatic processes in frequency conversion", Laser & Photonics Reviews **8**, 333–367 (2014).

[19] A. Messiah, *Quantum mechanics: volume ii* (North-Holland Publishing Company Amsterdam, 1962).

[20] S. F. Preble, Q. Xu, and M. Lipson, "Changing the colour of light in a silicon resonator", Nature Photonics **1**, 293–296 (2007).

[21]K. Kondo and T. Baba, "Dynamic wavelength conversion in copropagating slow-light pulses", Physical review letters **112**, 223904 (2014).

[22]A. M. Yacomotti, F. Raineri, C. Cojocaru, P. Monnier, J. A. Levenson, and R. Raj, "Nonadiabatic dynamics of the electromagnetic field and charge carriers in high-q photonic crystal resonators", Physical review letters **96**, 093901 (2006).

[23]M. Z. Alam, S. A. Schulz, J. Upham, I. De Leon, and R. W. Boyd, "Large optical nonlinearity of nanoantennas coupled to an epsilon-near-zero material", Nature Photonics **12**, 79–83 (2018).

[24]G. Woan, *The cambridge handbook of physics formulas*, eng (Cambridge University Press, Cambridge, 2000), p. 28.

[25]D. M. Sullivan, *Electromagnetic simulation using the fdtd method* (John Wiley & Sons, 2013).

[26]*Ansys lumerical: finite difference time domain (fdtd) solver introduction*, `https://support.lumerical.com/hc/en-us/articles/360034914633-Finite-Difference-Time-Domain-FDTD-solver-introduction` (visited on 05/05/2021).

[27]*Ansys lumerical: pml boundary conditions in fdtd and mode*, `https://support.lumerical.com/hc/en-us/articles/360034382674-PML-boundary-conditions-in-FDTD-and-MODE` (visited on 05/05/2021).

[28]*Ansys lumerical: periodic boundary conditions in fdtd and mode*, `https://support.lumerical.com/hc/en-us/articles/360034382734-Periodic-boundary-conditions-in-FDTD-and-MODE` (visited on 05/05/2021).

[29]J. D. Joannopoulos, S. G. Johnson, J. N. Winn, and R. D. Meade, *Photonic crystals: molding the flow of light (second edition)*, 2nd ed. (Princeton University Press, 2008), p. 20.

[30]*Ansys lumerical: convergence testing process for fdtd simulations*, `https://support.lumerical.com/hc/en-us/articles/360034915833-Convergence-testing-process-for-FDTD-simulations` (visited on 07/05/2021).

[31]D. M. Sullivan, *Electromagnetic simulation using the fdtd method* (John Wiley & Sons, 2013), p. 5.

[32]*Ansys lumerical: understanding the non-uniform mesh in fdtd*, `https://support.lumerical.com/hc/en-us/articles/360034382634-Understanding-the-non-uniform-mesh-in-FDTD` (visited on 08/05/2021).